

Optical Engineering

OpticalEngineering.SPIEDigitalLibrary.org

Successful starting point selection for two-mirror meniscus scanner optimization for laser machining

Vladimir I. Yurevich
Viacheslav Grimm
Igor Kananykhin
Sergey Gorny

SPIE.

Vladimir I. Yurevich, Viacheslav Grimm, Igor Kananykhin, Sergey Gorny, "Successful starting point selection for two-mirror meniscus scanner optimization for laser machining," *Opt. Eng.* **58**(1), 015109 (2019), doi: 10.1117/1.OE.58.1.015109.

Successful starting point selection for two-mirror meniscus scanner optimization for laser machining

Vladimir I. Yurevich,^{a,b,*} Viacheslav Grimm,^b Igor Kananykhin,^{a,b,c} and Sergey Gorny^{a,d}

^aLaser Center Ltd., St. Petersburg, Russia

^bITMO University, International Laboratory "Intelligent Optical Systems," St. Petersburg, Russia

^cCentral Research Institute of Laser Equipment and Technologies Ltd., St. Petersburg, Russia

^dPeter the Great St. Petersburg Polytechnic University, Institute of Metallurgy, Mechanical Engineering and Transport, St. Petersburg, Russia

Abstract. An algorithm for selecting the correct starting point for computer optimization of a two-mirror scanner with a meniscus lens is developed for use in laser machining. This algorithm performs joint analysis of aplanatism condition fulfillment and the field characteristics of the ghosts reflected from the meniscus surfaces back into the scanner mirror space. For integrity, all equations and estimates are given with respect to a major parameter: the curvature of the input surface. The second powerful tool for the optimization is the distance from the meniscus to the scanning mirrors, though its applicability is significantly limited by design considerations. Several scanner variants used to perform basic laser machining processes at various power levels are considered in detail. It is found that, for a fixed output numerical aperture, compacting the scanner always improves its optical performance. In general, compacting is an alternative to using scanners in systems with high-power laser sources. The results of this work are valid for any optical material and wavelength and are particularly relevant for systems based on CO₂ lasers, in which such scanners remain widely used. © The Authors. Published by SPIE under a Creative Commons Attribution 4.0 Unported License. Distribution or reproduction of this work in whole or in part requires full attribution of the original publication, including its DOI. [DOI: 10.1117/1.OE.58.1.015109]

Keywords: laser scanner; meniscus lens; back-focused ghosts; aplanatism; laser machining; optical simulations.

Paper 181073 received Jul. 25, 2018; accepted for publication Jan. 8, 2019; published online Jan. 30, 2019.

1 Introduction

Preobjective scanning systems are widely used in laser machines, because they combine very high-positioning speed with sufficiently high accuracy and relatively low cost. Typically, they consist of a two-mirror scanner and an optical system corrected for field curvature. The scanner nonlinearity and optical system distortion are noncritical problems, as they can be corrected successfully using electronics. In the scanning module for a CO₂ laser machine, the optical system often contains only a meniscus singlet, which is an integral component of most field flatteners.^{1,2} A meniscus singlet cannot generally provide perfect field curvature correction, being less effective than a multicomponent system. However, for a moderate output numerical aperture (NA), a meniscus singlet provides quite acceptable image quality over a field with a diagonal comparable to its effective focal length (EFL) because of the favorable relationship between the geometric aberrations and the large diffraction size (at 10.6- μm wavelength λ) of the focused beam. Thus, meniscus singlets are still used in laser systems with moderate NAs. Zinc selenide (ZnSe) is the main material used in the refractive optical components of commercial CO₂ laser machines. However, in addition to its high refractive index, the distinguishing features of this material are its high cost, the toxicity³ of the waste generated through its manufacturing/processing, and the large temperature coefficient⁴ of the refractive index. Consequently, reduction of the optical system size and component number is desirable, which also necessitates use of a meniscus singlet.

Despite the simplicity of such systems,⁵ optimization of a scanner with a meniscus singlet is difficult because of the

small number of variables. When all variables are freely assigned, the optimal configuration tends to yield a very thick meniscus⁶ with a localized entrance pupil, which is achieved by setting the distance between the scanner mirrors to approximately zero. This configuration targets maximum possible fulfillment of the sine condition on the output surface of the lens. It also significantly transforms the input angles, reducing the drop in geometric brightness at the field corners. However, the technical inconsistency of such a configuration is obvious and, in general, introduction of a finite intermirror distance and use of a technologically reasonable central thickness significantly decreases the optical quality of the system. Nevertheless, there are certain design parameter ranges that provide adequate quality while maintaining modest system weight and size. Optical designers utilize search algorithms⁷ to identify these ranges; however, these algorithms are not intuitive. As a result, without a correctly chosen starting point for numerical optimization of the system, the simulation programs provide opticians with various design parameter values within wide ranges, all providing approximately the same beam focusing quality. Further, no guidance on refining the quality is supplied. The optical quality of a system simulated using an incorrect starting point (where the starting point corresponds to the input parameters) may seem acceptable; however, the system design (which is based on the output parameters given by the above-mentioned simulations) is not optimal.

Additional optimization complexity arises from the problem of laser-induced scanner mirror damage. Even if a given starting point is successful in terms of optical quality, it is highly likely to be unacceptable because focused ghost reflections (FGRs) from the meniscus surfaces hit the scanner mirror surfaces.^{8,9} Tilting the lens surfaces¹⁰ does not eliminate the problem of FGR field interaction with the

*Address all correspondence to Vladimir I. Yurevich, E-mail: optic@newlaser.ru

mirror surface because of the considerable dimensions of the FGR field and mirror. This is a significant problem for systems involving high-brightness laser beams. Increased laser source brightness in the midinfrared spectral range is required to enhance the productivity of technological processes having laser processing of plastics, ceramics, glass, and carbon fiber reinforced polymer composites as the primary objective.¹¹⁻¹⁴ Therefore, the demand for powerful pulses in the infrared range has continued to grow. When first invented in the 1970s, transversely excited atmospheric CO₂ lasers¹⁵⁻¹⁷ were recognized as excellent laser technology tools. In addition, there have been consistent efforts to create commercial CO₂ lasers using different Q-switching techniques,¹⁸⁻²⁰ as well as self-injection pulsed lasers.^{21,22} This has facilitated manufacture of commercial CO₂ lasers emitting multikilohertz pulses with lengths of a few hundred nanoseconds and energies from tens to hundreds of millijoules, which significantly exceed the pulse energies of the most well-known fiber lasers.

FGR field interaction with the mirror surface is a considerable problem for a high-brightness CO₂ laser machine with ZnSe optical components. The typical parasitic reflection coefficients from the anti-reflection ZnSe surfaces are usually 0.2% to 0.3%,²³⁻²⁵ several times poorer than those of the glass and quartz surfaces of near-infrared optical components. Therefore, even with a 10-fold increase in diffraction size, the brightness of the beam reflected from the spherical surface of the meniscus and back-focused into the scanner mirror space can easily reach tens of megawatts per square centimeter, which inevitably induces mirror damage upon repetitive laser action. Further, ghost focus generators integrated into current optical simulation programs and ghost image analysis techniques²⁶ based on their application do not provide sufficient information on the FGR fields in scanning systems.

The primary objective of this study is to develop a detailed algorithm for finding a starting point for computer optimization, to provide the system with the optimal optical performance and prohibit focused ghost spots that could cause scanner mirror damage. This goal is achieved by combining computer modeling and geometric and matrix optics. The body of this paper is structured as follows. Section 2 describes the techniques and conditions employed in the numerical experiments and introduces the necessary techniques, input and output parameters, variables, and their normalizations. Section 3 discusses fulfillment of the

aplanatism conditions on the scanner meniscus surfaces. Section 4 presents a numerical simulation of the characteristics of the ghosts reflected from the meniscus surfaces back into the scanner mirror space. Analytically obtained equations for the FGR field size and position and the meniscus curvature, for which the FGR plane intersects the scanning mirror plane, are also presented. Section 5 summarizes the results from Secs. 3 and 4 and gives examples of starting point selection for optimization of scanners with different parameters; the considered scanners are typically used in laser machines for common applications. Finally, Sec. 6 provides a brief conclusion based on the research results.

2 Model of Two-Axis Laser Scanner with Meniscus Lens

2.1 Typical System Configuration and Parameters

The optical layout of a two-axis scanner with a meniscus lens is shown in Fig. 1. Two movable galvo mirrors M_1 and M_2 (where M_1 and M_2 simultaneously denote the scanner mirrors themselves and their half-sizes with respect to the rotation axis) provide laser beam deflections along the x and y axes. The distances from the meniscus input surface to the mirrors M_1 and M_2 are m_1 and m_2 , respectively. The distance between the mirrors $|m_1 - m_2|$ is commonly called $x - y$ separation. A meniscus lens with input curvature c_1 , output curvature c_2 , refractive index n , central thickness T , and EFL f' (optical power $\Phi = 1/f'$) is used to focus the stirred beam. This creates a rectangular processing field with maximum half-sizes X_i and Y_i reached at maximum scan angles $\pm\theta_{S1 \max, S2 \max}$. The angular position θ of a mirror is given by the sum of the initial adjustment angle θ_0 and the scanning angle $\pm\theta_{S1, S2}$. The θ_0 of M_2 is always 45 deg. To reduce the $x - y$ separation, the rotation axis of M_1 has an additional tilt θ_{12} , bringing its edge as close to the reflecting surface of M_2 as possible,^{27,28} as illustrated in Fig. 1(b). Therefore, the θ_0 of M_1 is not 45 deg, unlike in older systems.

The optimal shapes of M_1 and M_2 are the elliptical and paddle blades, respectively,^{27,29} with the latter being asymmetric with respect to its rotation axis. Mirror shape optimization and size reduction are necessary to reduce both the moments of inertia and $x - y$ separation of the mirrors. To simplify the manufacturing, these shapes are sometimes reduced to rectangles with straight-cut or rounded corners.³⁰ Typically, manufacturers rank mirrors based on

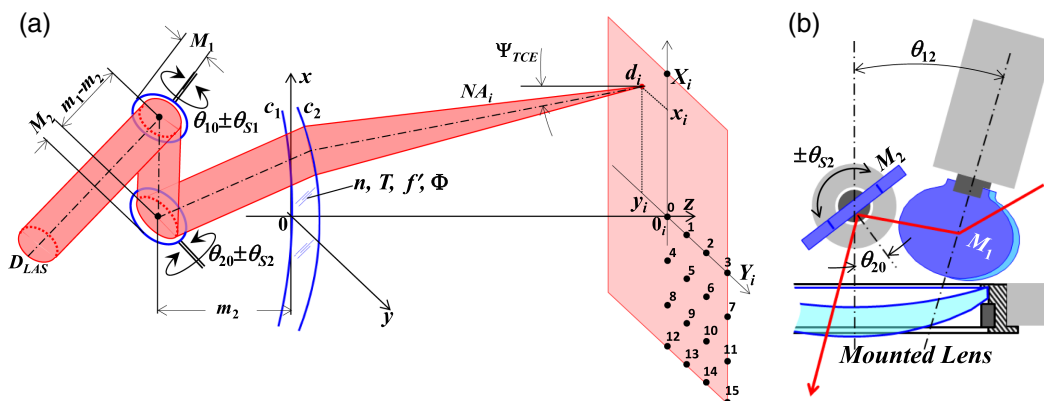


Fig. 1 (a) System parameters; see text for parameter descriptions and (b) typical scan mirror positions.

some arbitrary aperture A for a raw laser beam, which is expressed in array form, e.g., $A \in (5, 8, 10, 12, 15, 20, 25, 30, 40, 50, \dots)$ mm. There is no strict mirror size standard that corresponds to a particular value of A , but the following relations are usually adequate: $|m_1 - m_2| \approx 1.25A$ (m_1 and m_2 are shown in Fig. 1), $M_1 \approx 0.9A$, and $M_2 \approx 0.8A$.^{27,29,31} It is important to note that the properties related to the apodization factor, size, and measurement methods of the beam entering A are never specified. Therefore, the choice of A from the above-mentioned array is based on prior expertise.

2.2 Numerical Experiment Technique, Input Parameters, and Variables

In this study, a number of numerical experiments were conducted to form a large dataset of input information necessary for further analytical estimates. Focusing quality of the scanner was studied in ZEMAX software using a mixed sequential/nonsequential ray tracing mode. Optical layout included meniscus lens and two mirrors rotated about their vertices. Rotation was set using the multiconfiguration editor. The analyzed systems were optimized for the best Strehl ratio and/or for the minimum root-mean-square (RMS) spot radius. The relationship between the clear mirror aperture A and raw laser beam diameter D_{LAS} is uncertain; therefore, the laser intensity distribution was assumed to be uniform, which enabled the conditional equality $D_{\text{LAS}} = A$ to be set. In all experiments, the angles $\pm\theta_{S1 \text{ max}, S2 \text{ max}}$ were ± 9 deg, close to the scan angle limits for most galvos.^{27,28,31–33} The λ value was $10.6 \mu\text{m}$, and the meniscus material was ZnSe.

For mathematical coherence, all calculations described below were performed considering the sign convention adopted in optics. The origin was placed at the vertex of the input meniscus surface. Note that it is reasonable to choose the output numerical aperture NA_i and $\Phi = f'^{-1}$ as the input optical parameters of the system. Indeed, the system user can typically inform the system designer of the desired process resolution and processing field size only, and these data are quite sufficient for preliminary estimates. As a rule, the material response size does not coincide with the focused laser beam size. Therefore, the relationship between these two quantities must be found experimentally using any available optics. Consequently, the designer obtains the output NA of the system from the relation $NA_i = K\lambda d_i^{-1}$, where K is a coefficient depending on the optical intensity distribution over the entrance pupil and d_i is the diameter of the focused beam, providing the required material response size. For rough estimates, $K \sim 1$ is well suited. The required maximum processing field size $2F = \max(2X_i, 2Y_i)$ determines the meniscus EFL. For the maximum telecentricity error Ψ_{TCE} and $\pm\theta_{S1 \text{ max}, S2 \text{ max}}$ not exceeding ± 10 deg, the estimate $f' = 3F$ is very reasonable. The raw beam diameter providing the required NA at a given EFL can be estimated using $D_{\text{LAS}} = 2NA_i\Phi^{-1}$. In turn, D_{LAS} determines the sizes of the mirrors and the minimum possible $x-y$ separation. The one is minimized because of the need to improve the optical quality of the scanner, which axiomatically reaches the maximum in the ideal situation when $x-y$ separation is zero. For generality, hereinafter all curvatures were normalized to Φ and the linear dimensions were normalized to EFL.

In terms of the primary objective of this study, the major independent variables are c_1 and m_2 . In calculations, they are supplemented by the system parameters NA_i and Φ as well as by the set of the mirror unit design characteristics (M_1 , M_2 , and m_1). The above-mentioned variables are confounding. Characteristics of the mirror unit implicitly affect the optical quality of the system and explicitly limit the permissible range of c_1 owing to the FGRs influence. In contrast, design characteristics of the mirror unit cannot be randomly assigned because they are implicitly depended on NA_i and the overall meniscus size.

3 Spontaneous and Optimized Aplanatization of Scanner Meniscus

Numerical simulations examining the optical quality of scanners with EFLs of 100, 300, and 600 mm and $2F$ of 65, 200, and 400 mm were performed. A constant $NA_i = 0.03$ was obtained by synchronous varying both EFLs and the raw beam sizes. This NA is close to the limit for a singlet, providing acceptable focusing quality over a large field. The c_1 values were taken from a range from -3EFL^{-1} to 0. The EFL of each scanner was kept constant. It induced a noticeable change in the back focal distance caused by the principal planes displacement when the meniscus was changed from a dome lens to a planoconvex lens, as well as the introduction of correct defocus when searching for the plane of least confusion. In all simulations, the $x-y$ separations were taken the shortest possible for a pairs of mirrors XY7.5F, XY20G, and XY40G²⁹ and were 9, 24, and 60 mm, respectively. In the first set of simulations, the $|m_2|$ distances were also fixed at the minimum possible values of 19, 60, and 100 mm. They were assigned based on design considerations (M_2 , the input surface sag, and the probable lens mount design) as well as practical experience. The value of c_2 was optimized for the input data listed above. With an error $< 1\%$, optimization results can be estimated as $c_2 = 0.94c_1 - 0.73\Phi$. The focusing quality curves obtained by optimizing c_2 for a fixed distance m_2 are shown in Fig. 2(a) by solid lines. Then m_2 was set as a variable and its optimization was performed for the c_1/c_2 pairs previously obtained. The focusing quality curves for scanners with optimized m_2 are shown in the same figure by dotted lines. In both cases, the focusing quality over the processing field was estimated from the Strehl ratios averaged over 16 points in one of its quadrants, as shown in Fig. 1. The absolute values for the scanner parameters are listed on the right side of Fig. 2(a) because, when normalized, they appear identical.

The curves reveal a significant decrease in the optical quality of scanners with fixed m_2 for steep and flat menisci. For a certain range of meniscus curvatures, the optical quality of a system with a fixed m_2 is identical to that of a system optimized for that position. The c_1/Φ value corresponding to maximum optical performance is unchanged when the scanner parameters are scaled. Because all primary aberrations are presented in the scanner, the curves should be analyzed rigorously by calculating all the Seidel sums.^{34,35} This approach leads to bulky equations impeding engineering estimates. However, a simple estimate fulfilling the aplanatism conditions on the meniscus surfaces is well suited to finding the position corresponding to the maximum optical performance. The aplanatism conditions are strictly fulfilled

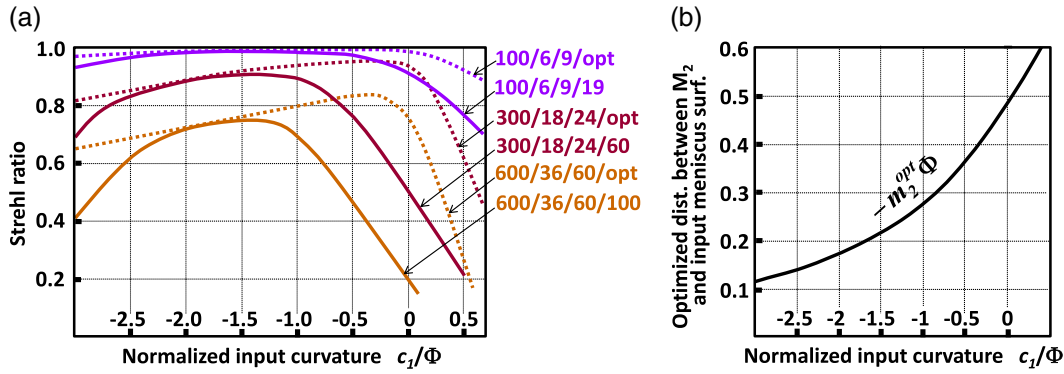


Fig. 2 Optical performance of scanners with $NA_i = 0.03$. (a) Simulated Strehl ratios averaged over processing field for scanners with fixed (solid lines) and optimized (dotted lines) m_2 . The curve labels have the format $f'/D_{LAS}/x - y$ separation/ $|m_2|$. (b) Dependence of optimized m_2 on c_1 .

only for the chief rays. Most of the rays of the beam cannot fulfill the condition, so these rays will have aberrations as we move from the chief rays to ray bundles and then to wide oblique beams. Such transition drastically corrupts applying the theoretical underpinnings of aplanatism. Nevertheless, the concepts of aplanatism and aplanatic surfaces are widely used in practical optics.^{2,36,37} These surfaces are classified as concentric (also called aplanatic surfaces of the first kind^{36–38} or surfaces with normal incidence³⁴) and strictly aplanatic (also called aplanatic surfaces of the second kind). The use of such surfaces in optical design leads to concentric—concentric (or aplanatic—aplanatic) shapes for steep curvatures and to aplanatic—concentric shape for flat curvatures. It should be emphasized that using the term “aplanatism” for scanning systems optimization is greatly condition. Seidel coefficients analysis indicates that optimized surfaces getting from ray tracing computations become nearly concentric and nearly aplanatic and work as follows: The offence against the aplanatic conditions on the input surface introduces some small spherical aberration, some coma, and considerable astigmatism. In turn, the offence against the concentric conditions on the output surface introduces the same aberrations but of opposite sign. There is no complete annihilation of aberrations of the same names even for those menisci configurations, which are the best optimized, because the subtracted values have different magnitudes. Nevertheless, even for wide input beams, the size of aberrational spot diagrams in the plane of the least confusion is comparable with the diffraction size.

At the central zone of the entrance pupil, the concentric and aplanatic curvatures for the lens input surface have the forms:

$$c_{1C} = P^{-1} \tag{1}$$

and

$$c_{1A} = [(n + 1)P]^{-1}, \tag{2}$$

respectively, where P is the distance from the center of the entrance pupil to the origin, $P = (m_1 + m_2)/2$. This P is averaged because it oscillates between the mirrors in the m_1 to m_2 range during the scanning process. However, incorporating this uncertainty greatly complicates the subsequent calculations and provides no benefit, as all associated estimation errors are eliminated during the optimization.

Thus, this uncertainty is neglected as a matter of principle in the context of further computer optimization. The aplanatic curvatures of the output meniscus surface are found using the Abbe invariant and have more complex forms:

$$c_{2C} = \left[\frac{n}{P^{-1} + (n - 1)c_1} - T \right]^{-1} \tag{3}$$

and

$$c_{2A} = \frac{1}{(n + 1)} \left[\frac{1}{P^{-1} + (n - 1)c_1} - \frac{T}{n} \right]^{-1}. \tag{4}$$

Figure 3(a) displays the dependence of these curvatures together with the ray traced curvature c_2 on the c_1 values plotted for generalized scanner parameters $|m_1 - m_2| = 0.08/\Phi$ and $T = 0.03/\Phi$. The $|m_2|$ distance was kept constant at the value of $0.20/\Phi$. The graph of c_1 as a function of c_1 is given for clarity. It is seen that on keeping m_2 constant, with a monotonic increase in the input curvature of the meniscus, one of its surfaces alternately satisfies the aplanatism conditions, as indicated by the dots at the intersections of the graphs in Fig. 3(a). For typical scanner geometries, the condition in Eq. (1) is fulfilled for very steep menisci; therefore, it is not addressed further here.

Such spontaneous aplanatization explains the value of the input curvature \overline{C}_1 corresponding to maximum optical performance of the scanners in Fig. 2(a), which is the mean of the c_1 -roots of Eqs. (3) and (4), i.e., $\overline{C}_1/\Phi = (2\Phi)^{-1}(c_{2C} + c_{2A})$. For this calculation, c_2 should be expressed in terms of c_1 , and for simplicity, the term containing the square of the curvature is neglected, yielding

$$\frac{\overline{C}_1}{\Phi} = \frac{2n + 1 + 2(n - 1)(P\Phi)^{-1}}{3(n - 1)}. \tag{5}$$

For the simulated scanners, the value of \overline{C}_1/Φ given by Eq. (5) is ~ -1.5 , which agrees well with the maximums of the solid curves in Fig. 2(a). The width of the maximum optical quality range for a system with a fixed entrance pupil is obtained by subtracting Eq. (3) from Eq. (4). Similar calculations and simplifications yield:

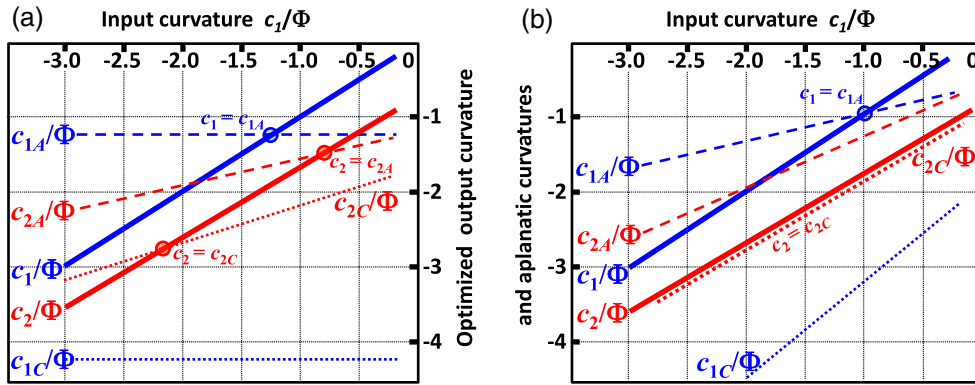


Fig. 3 Dependence of the optimized output curvatures (solid-red lines) and aplanatic curvatures (dotted and dashed lines) on the input curvature for the systems with (a) fixed and (b) optimized position of the entrance pupil. The graphs of c_1 as a function of c_1 (solid-blue lines) are given for clarity.

$$\frac{\delta C_1}{\Phi} = -\frac{1 + (P\Phi)^{-1}}{2}. \quad (6)$$

Equation (6) gives the width of the maximum optical quality range, which is approximately 2.

Further optimization of the scanner was made by setting m_2 variable. All other parameters of the system were the same as those used in the previous calculations. The dependence of the optimized m_2 on c_1 is shown in Fig. 2(b). In this case, the output meniscus surface becomes nearly concentric about the entrance pupil for all possible input curvatures as depicted in Fig. 3(b). Therefore, the range of system parameters providing good optical performance expands from extremely steep to fairly flat meniscus lenses, as indicated by the dotted curves in Fig. 2(a). However, in reality, the ability to decrease m_2 for a steep meniscus is limited by the sag, lens mount design, motor size, and x -mirror protrusion over the y -mirror edge [see Fig. 1(b)]. In contrast, lengthening m_2 with meniscus flattening induces an increase in its clear aperture, which consistently increases the technologically reasonable T and quadratically enlarges the meniscus overall, as well as the material capacity. The relationships in Eqs. (5) and (6) are sufficient for choosing the optimization starting point for a system with a low-power laser source. However, for high-power laser sources, this choice is complicated significantly by considering the locations of the FGR fields in the mirror space of the scanning system.

4 Characteristics of Back Focused Ghost Reflections

4.1 Numerical Simulation of Characteristics of Back-Focused Ghosts and Their Fields

FGR field formation is governed by the same principles as processing field formation. In the following calculations, the scanning angles on both axes were assumed to be identical for compactness, allowing consideration of the square processing field using a one-dimensional approximation. In this case, the coordinates of the scanning point x_i , y_i and maximum half-sizes X_i , Y_i can be replaced with the coordinate ξ_i and half-size Ξ_i , respectively. Up to the small error caused by the scanner nonlinearity and lens distortion, the FGR field from the j 'th meniscus surface is also a square with the spot coordinate ξ_j and maximum half-size Ξ_j , according to the invariant:

$$\Xi_j NA_i = \Xi_i NA_j. \quad (7)$$

Correspondingly, all normalized coordinates are equal, i.e., $\xi_i/\Xi_i = \xi_j/\Xi_j = \theta_s/\theta_{s \max}$.

Computer simulation of the FGR field characteristics were conducted for the c_1/c_2 pairs as well as for the x - y separations and m_2 distances previously used in Sec. 3 in examining scanners with a fixed m_2 . The ghost field size and location were measured in the plane with the best Strehl ratio averaged over the total ghost field. The FGR fields tightly fill the space of the probable scanner mirror location, as indicated in Fig. 4(a).

The connecting lines in Fig. 4(a) indicate combinations of FGR fields from both surfaces of an optimized meniscus. The FGR fields from the more curved output surface are located closer to the meniscus. Those from the smoother input surface leave the scanner mirror space more quickly with its flattening. However, even for a flat or slightly convex input surface, the FGRs from the output surface are located in the probable scanner mirror space. Typical scanner mirror locations drawn to scale are also shown in Fig. 4(a). The uncertainty of the mirror positions in the figure is caused by lack of rigorous scaling of the actual scanner dimensions while changing the input raw beam size. Unlike the case of a multicomponent optical system, the dimensions of the FGR fields from both surfaces of the optimized meniscus were found to be practically identical at the same axial coordinate. Moreover, for each surface, the absolute value of the normalized FGR plane coordinate coincided with the normalized FGR field size with an accuracy sufficient for the estimation, i.e., $-z_j\Phi \approx \Xi_j/\Xi_i$ [see Fig. 4(b) and the Appendix].

For typical scanner design parameters, the NAs of the FGRs from the meniscus surfaces are related to the NA in the image space, as $NA_1 = (3 \dots 6)NA_i$ and $NA_2 = (8 \dots 12)NA_i$. The layout of an arbitrary scanner configuration is shown in Fig. 5(a). For a variety of scanning angles $\pm\theta_{s1}$ and fixed θ_2 , the intersection of the FGR plane with the mirror surface gives a smooth curve with a chord parallel to the scan axis of M_2 . In turn, scanning M_2 produces a variety of these curves corresponding to a set of angles $\pm\theta_{s2}$, as shown in Fig. 5(b). In this space, the probability of local mirror coating damage is very high. Every local damage spot becomes a powerful source of heat dissipation and sputtering of the damage products onto neighboring areas of the surface. Thus, the process is cumulative and

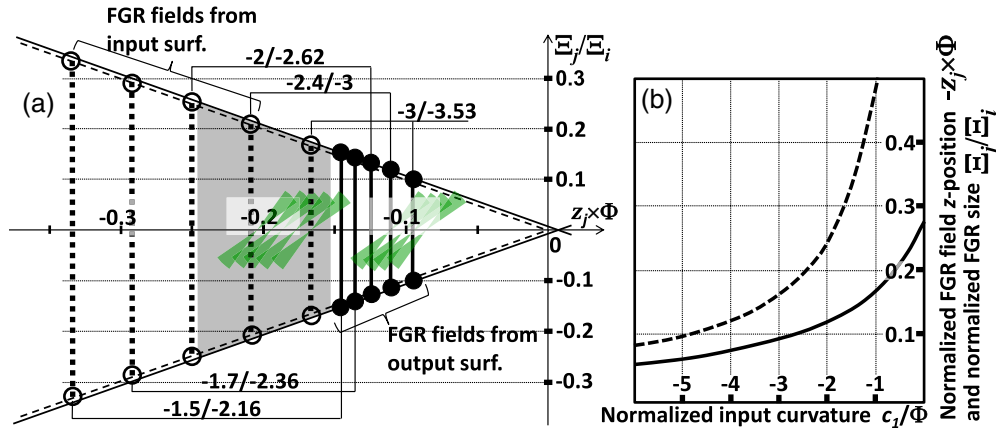


Fig. 4 Generalized results of computer simulation of FGR field characteristics in scanner mirror space. (a) Positions and transverse sizes of FGR fields. The dashed/hollow and solid dumbbells represent the FGR fields from the input and output meniscus surfaces, respectively. The numbers above the connecting lines correspond to the optimized c_1/c_2 pairs in units of Φ^{-1} . The shading shows the dense FGR field region from the output surface for $c_1/\Phi < -1.5$. Typical scanner mirror locations are shown to scale. (b) Dependence of FGR fields z-position and transverse size on meniscus input curvature. As on the left, the dashed and solid lines correspond to the input and output surfaces, respectively.

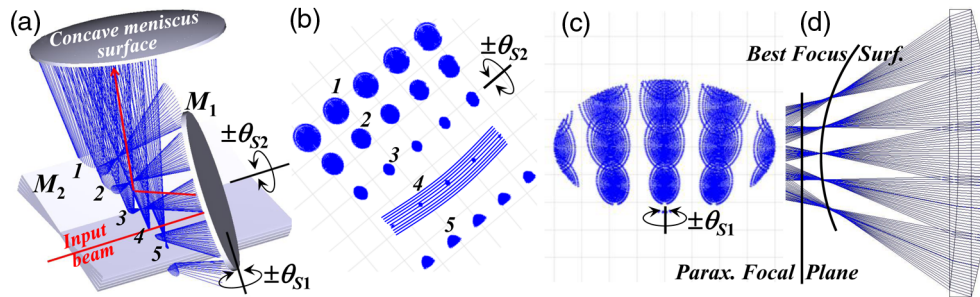


Fig. 5 (a) Scanner layout, deliberately modeled so that FGR plane crosses M_2 . (b) FGR spots on M_2 , where blue smooth curves indicate FGR plane intersections with mirror surface. The numbers near the spots correspond to the FGR beams selected from (a). (c) FGR spots on M_1 . (d) Introduction of defocus while searching for minimum FGR spot size.

ends quickly with complete mirror damage because of the powerful overheating of the substrate. Figure 5(c) demonstrates that the FGR spots do not strike M_1 in the chosen configuration.

Computer simulation of the FGR location and spot size is very time-consuming, because the paraxial FGR plane degenerates into a sphere-like three-dimensional best focus surface with increasing FGR NA, as shown in Fig. 5(d). Therefore, it is necessary to introduce a unique defocus value for each analyzed spot in the FGR field. The results of computer simulations of the beams creating the FGR field are presented in Fig. 6. The patterns in each cell show the dependence of the RMS beam radius at the FGR best focal spot on the input angle, for scanner output NAs ranging from 0.015 to 0.03. To study the FGR behavior, the scanner geometry was changed such that m_2 was varied while the x - y separation was kept constant at its minimum possible value. Note that the y -dimensions of the cells are expressed in units of $1/NA_1 \mu\text{m}$. This measure was chosen because NA_1 and NA_2 change with the curvature of the meniscus surface when the scanner output NA is kept constant. The striped and solid regions correspond to FGRs from the input and output surfaces, respectively. The upper and

lower boundaries of each pattern correspond to output NAs of 0.03 and 0.015, respectively. Degeneration of a pattern into a line indicates that, for the entire range of input angles, FGR focusing occurs with the diffraction quality. For flat menisci, the FGR fields from the input surface quickly exit the reasonable scanner mirror location range; therefore, the corresponding patterns are missing from the rightmost cells of Fig. 6. For all meniscus configurations, it is apparent that the back-focusing quality deteriorates at the field margins; however, it is always close to the diffraction limit at small input angles. In addition, by analogy with the curves in Fig. 2(a), a high-quality focusing of the ghosts in the entire range of input angles takes place near some c_1/c_2 pairs, determined by the distance from the meniscus to the scanner mirrors. With increasing scanner dimensions, the region of a high-quality focusing of the ghosts from both surfaces drifts toward the region of smaller curvatures. Because of the noticeable dissonance between these drifts for both meniscus surfaces, high-quality ghosts focusing occurs in the scanner mirror space for at least one of the meniscus surfaces for all scanner configurations over practically the entire curvature and input angle ranges. In this case, the RMS beam radius of the focused ghosts varies from 17 to

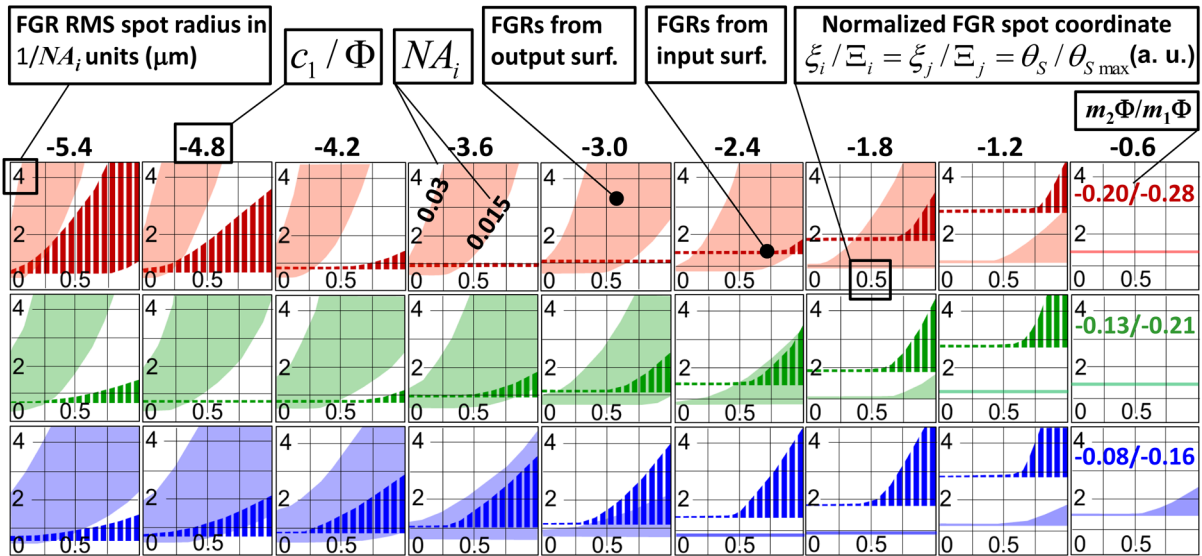


Fig. 6 FGR RMS spot radius versus scanner output NA and normalized FGR spot transverse coordinate. The scanner output NA varied from 0.03 (upper boundary of each pattern) to 0.015 (lower boundary). The striped and solid patterns correspond to FGRs from the input and output surfaces, respectively. The normalized meniscus input curvatures c_1/Φ are given above the cells. The scanner parameters are in the format $m_2\Phi/m_1\Phi$ and shown on the right. The maximum scan angle $\theta_{S\max}$ is 9 deg.

100 μm , yielding a power density range of 10^6 to 3.5×10^7 W/cm^2 . This estimate is valid for 40-mJ pulse energy, 200-ns pulse width, and 0.2% parasite reflection. This intensity is quite sufficient to damage the mirror surface at high repetition rates.

The simulation results show that, for medium-power laser sources, the possibility of locating the FGR fields in the scanner mirror space should be subject to the ghost brightness computation and comparison of the calculated values with the declared mirror damage threshold. For high-power systems, the scanner configuration should completely eliminate the possibility of back-focusing on the scanner mirror surfaces.

4.2 Analytical Model of Back-Focused Ghost Field Formation

The aim is to develop an algorithm for correct starting point selection for computer optimization of the scanner, yielding the maximum possible optical performance and without FGRs in the mirror space. To achieve this, the results obtained above should be supported by analytical expressions for the FGR position and size in a form amenable

to engineering estimations. The associated calculations are explained by the scheme in Fig. 7(a).

It is obvious that, accurate to the defocus, the z -coordinate of the FGR plane from the first surface of the meniscus is half the radius of curvature:

$$z_1 = (2c_1)^{-1}. \quad (8)$$

To find the FGR NA from the first surface, $NA_1 = -D_{\text{LAS}}/2z_1$, we express the size of the input beam in terms of the output NA of the system, $D_{\text{LAS}} = 2NA_i\Phi^{-1}$, which yields

$$NA_1 = -2NA_i c_1 \Phi^{-1}. \quad (9)$$

Substituting Eq. (9) into Eq. (7) yields the FGR field size from the first surface of the meniscus:

$$\Xi_1 = -\Xi_i \Phi (2c_1)^{-1}. \quad (10)$$

The position and size of the FGR from the second surface are most easily found from ABCD matrix analysis³⁹ for a ray propagating through a lens, being reflected from the second surface and returning:

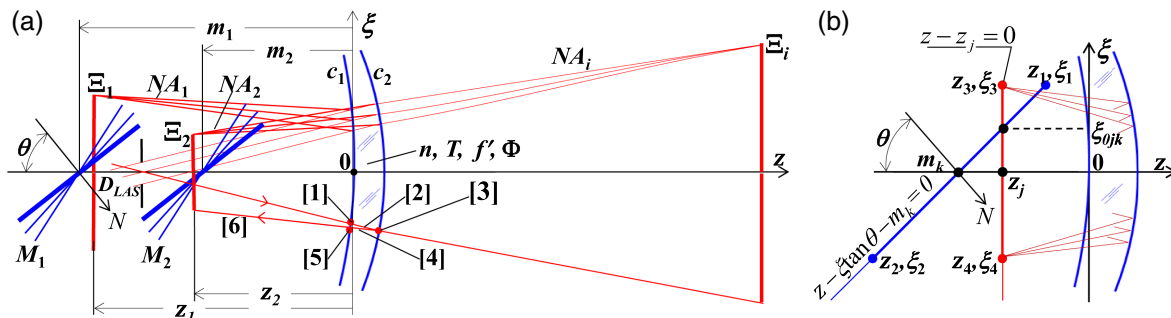


Fig. 7 (a) FGR field formation and (b) intersection between FGR and mirror planes.

$$M = \begin{bmatrix} A & B \\ C & D \end{bmatrix} = [6] \cdot \begin{bmatrix} A' & B' \\ C' & D' \end{bmatrix},$$

where $\begin{bmatrix} A' & B' \\ C' & D' \end{bmatrix} = [5] \cdot [4] \cdot [3] \cdot [2] \cdot [1].$ (11)

The 2×2 matrices [1] to [6] describe the sequence of refractions, reflections, and transfers indicated in Fig. 7(a). Considering the standard form of these matrices, we have

$$M = \begin{bmatrix} 1 & -z_2 \\ 0 & 1 \end{bmatrix} \cdot \begin{bmatrix} 1 & 0 \\ (1-n)c_1 & 1 \end{bmatrix} \cdot \begin{bmatrix} 1 & T/n \\ 0 & 1 \end{bmatrix} \cdot \begin{bmatrix} 1 & 0 \\ 2nc_2 & 1 \end{bmatrix} \cdot \begin{bmatrix} 1 & T/n \\ 0 & 1 \end{bmatrix} \cdot \begin{bmatrix} 1 & 0 \\ (1-n)c_1 & 1 \end{bmatrix}. \quad (12)$$

The introduction of a matrix with primes is explained by the fact that the coefficient C' gives the round-trip EFL of the meniscus:

$$\Phi_{\leftrightarrow} = -C' = -\left[2c_1 - 2n(c_1 - c_2) + \frac{2(1-n)^2}{n} Tc_1^2 + 4(1-n)Tc_1c_2 + \frac{2(1-n)^2}{n} T^2c_1^2c_2 \right]. \quad (13)$$

In Eq. (13), without noticeable loss of accuracy, the terms containing the square and cube of the curvature can be neglected. Thus, expressing c_2 in terms of c_1 yields:

$$\Phi_{\leftrightarrow} = \frac{2n\Phi}{n-1} - 2c_1 - 4T\Phi c_1. \quad (14)$$

$$z_2 = \frac{1 + \frac{2(1-n)T}{n}c_1 + 2Tc_2 + \frac{2(1-n)T^2}{n}c_1c_2}{2c_1 - 2n(c_1 - c_2) + \frac{2(1-n)^2}{n}Tc_1^2 + 4(1-n)Tc_1c_2 + \frac{2(1-n)^2}{n}T^2c_1^2c_2}. \quad (18)$$

Equation (18) provides no more than 0.02% error relative to the computer simulation results. This small error is obtained because this expression does not account for the defocus. Based on perturbation theory analysis of Eq. (18), it is possible to ignore most terms containing squares and cubes of the curvature. Hence

$$z_2 = \frac{1 + \frac{2(1-n)T}{n}c_1 + 2Tc_2}{2c_1 - 2n(c_1 - c_2) + 4(1-n)Tc_1c_2}. \quad (19)$$

Further analysis shows that, without loss of accuracy, it is possible to remove the second term from the numerator and the last term from the denominator simultaneously. Removing these terms and expressing c_2 in terms of c_1 finally yields:

$$z_2 = \frac{\frac{(n-1)}{2} + [(n-1)c_1 - \Phi]T}{(n-1)c_1 - \Phi n}. \quad (20)$$

Equation (20) provides an error of ~8% for a steeper meniscus lens surface and practically zero error for flat surfaces relative to the computer simulation results.

The beam size varies insignificantly as it makes a round trip through the meniscus. Assuming that it is constant and using the invariant $NA_2\Phi_{\leftrightarrow}^{-1} = NA_1\Phi^{-1}$, the FGR NA from the second surface is

$$NA_2 = 2NA_1 \left(\frac{n}{n-1} - \frac{c_1}{\Phi} - 2Tc_1 \right). \quad (15)$$

Substituting Eq. (15) into Eq. (7) yields the size of the FGR from the second meniscus surface:

$$\Xi_2 = \frac{\Xi_i}{2 \left(\frac{n}{n-1} - \frac{c_1}{\Phi} - 2Tc_1 \right)}. \quad (16)$$

From the full matrix product [Eq. (12)], we need only the coefficient A , for which equality to zero means that all rays entering the system at the same angle are focused at one point. Despite the simplicity of the original matrices, the final expression for A has a rather complex form:

$$A = \left[1 + \frac{2(1-n)T}{n}c_1 + 2Tc_2 + \frac{2(1-n)T^2}{n}c_1c_2 - z_2 \left[2c_1 - 2n(c_1 - c_2) + \frac{2(1-n)^2}{n}Tc_1^2 + 4(1-n)Tc_1c_2 + \frac{2(1-n)^2}{n}T^2c_1^2c_2 \right] \right]. \quad (17)$$

Accordingly, the expression for the coordinate of the FGR plane from the second surface is hardly suitable for engineering estimates:

As illustrated in Fig. 7(b), in the one-dimensional model considered here, the mirror plane is replaced by the line segment $[(z_1, \xi_1), (z_2, \xi_2)]$, lying in the plane of incidence and defined by the two-point straight-line equation:

$$z - \xi \tan \theta - m_k = 0, \quad (21)$$

where $k = 1, 2$ refers to the mirror number. By analogy, the FGR plane is replaced by the line segment $[(z_3, \xi_3), (z_4, \xi_4)]$, lying in the same plane and defined by the line equation:

$$z - z_j = 0. \quad (22)$$

For convenience, the ξ -solution of the system of Eqs. (21) and (22) is considered in the subsequent calculations. The ξ -coordinate of the intersection point of the lines described by Eqs. (21) and (22) is

$$\xi_{0jk} = (z_j - m_k) \tan^{-1} \theta, \quad (23)$$

where $\theta = \theta_0 + \theta_5$ is the sum of the mirror surface tilts providing the maximum projection of the $[(z_1, \xi_1), (z_2, \xi_2)]$

segment onto the z -axis. To have the lines intersect inside the above-mentioned segments, simultaneous fulfillment of the following conditions is necessary:

$$\max(\xi_2, \xi_4) \leq \xi_{0jk} \leq \min(\xi_1, \xi_3). \quad (24)$$

The small inclination of the first mirror [Fig. 1(b)] and slightly nonplanar shape of the FGR best focus surface [Fig. 5(d)] do not significantly violate the problem symmetry. By assuming $z_3 = z_4 = z_j$, $\xi_4 = -\xi_3$, the inequalities [Eq. (24)] can be rewritten using the coordinates of the mirrors and FGR field edges:

$$\begin{aligned} \max(-M_k \sin \theta, -\Xi_j) &\leq (z_j - m_k) \tan^{-1} \theta \\ &\leq \min(M_k \sin \theta, \Xi_j). \end{aligned} \quad (25)$$

Fulfillment of the inequalities [Eq. (25)] implies that the FGR field from the j 'th surface of the meniscus crosses the k 'th mirror at some point. Substituting z_j from Eqs. (8) and (20) and Ξ_j from Eqs. (10) and (16), Eq. (25) can be transformed to find the forbidden ranges of c_1/Φ in terms of the scanner input parameters:

$$\begin{aligned} &\left[\frac{1}{2\Phi(m_k + M_k \sin \theta)}, \frac{1}{2m_k} \left(\frac{1}{\Phi} + \Xi_i \tan \theta \right) \right] \\ \max \leq \frac{c_1}{\Phi} \leq \min &\left[\frac{1}{2\Phi(m_k - M_k \sin \theta)}, \frac{1}{2m_k} \left(\frac{1}{\Phi} - \Xi_i \tan \theta \right) \right] \end{aligned} \quad (26)$$

and

$$\begin{aligned} &\left[\frac{n(m_k + M_k \sin \theta - T/n) + \frac{1}{2}(n-1)\Phi^{-1}}{(n-1)(m_k + M_k \sin \theta - T)}, \frac{\frac{1}{2}(n-1)(\Phi^{-1} + \Xi_i \tan \theta) + (m_k n - T)}{(n-1)(m_k - T)} \right] \\ \max \leq \frac{c_1}{\Phi} \leq \min &\left[\frac{n(m_k - M_k \sin \theta - T/n) + \frac{1}{2}(n-1)\Phi^{-1}}{(n-1)(m_k - M_k \sin \theta - T)}, \frac{\frac{1}{2}(n-1)(\Phi^{-1} - \Xi_i \tan \theta) + (m_k n - T)}{(n-1)(m_k - T)} \right]. \end{aligned} \quad (27)$$

The two sets in Eq. (26) and the two sets in Eq. (27) refer to the intersections of both scanner mirrors with the FGR fields from the meniscus input and output surfaces, respectively. The cardinality of these sets depends on the scanner geometry. It is governed by NA_i , which determines the mirror sizes and the x - y separation through the input beam size, and by the processing field size Ξ_i , which determines the minimum possible EFL of the meniscus Φ^{-1} . In general, the sets in Eq. (27) have strictly greater cardinality than those in Eq. (26).

5 Selection of Starting Point for Optimization of Scanners Used in Basic Laser Machining Processes

The optimization criteria are the maximum focusing quality over the entire processing field, FGR control in the scanner mirror space, and the minimum focusing meniscus size. The only obvious optimization issue is that, although minimizing the x - y separation improves the optical quality of the system and minimizing all distances reduces its size, moving the scanner mirrors closer to the meniscus requires an increase in its curvature. This, in turn, induces synchronous movement of the FGR fields in the same direction. Thus, there is a trade-off between the optical performance and size of the scanner. Consequently, the starting curvature of the input surface should be chosen such that the aplanatism conditions [Eqs. (5) and (6)] are satisfied, but the starting curvature does not fall into the ranges of the forbidden values [Eqs. (26) and (27)]. Further joint solution of the mentioned equations provides no visible results and is of mathematical interest only. Therefore, graphical interpretations of some cases of practical significance are presented here.

The greatest difficulty in choosing an optimization starting point is encountered when employing scanners delivering high-brightness radiation to the processing area; such

scanners are used for single-pass cutting of thick organic materials, multipass cutting, structuring, and thermal decomposition of brittle materials.^{11-14,40-44} In these processes, a large processing field is combined with a high output NA. The corresponding diagram for choosing the optimization point of such a scanner, with $\Xi_i = 0.33\Phi^{-1}$ and $\text{NA}_i = 0.03$, is shown in Fig. 8.

Each curve represents the computed Strehl ratios averaged over the processing field for a given scanner geometry, for a meniscus with input curvature plotted along the x -axis and optimized output. The horizontal bars indicate the forbidden input curvature ranges calculated using Eqs. (26) and (27). The $M_k S_j$ notation on the bars indicates that the plane of the k 'th mirror is intersected by the FGR field from the j 'th meniscus surface. Accordingly, the allowed curvature ranges for each scanner configuration correspond to the locations where there are no bars. The dashed vertical lines are the aplanatism estimates given by Eq. (5). It is apparent from the figure that, for high-power systems, only large scanners with flat menisci can be reliably used. Reducing $|m_2|$ from 0.33 to $0.2\Phi^{-1}$ narrows the allowed curvature range by a factor of approximately three, but scanners with the maximum possible Strehl ratio for the given geometry still fall within the range. With further reduction of $|m_2|$ to $0.13\Phi^{-1}$, an optimization starting point can be found near a c_1/Φ value of ~ -1.75 . The optical performance of the scanner remains maximized; however, the FGRs from the meniscus output surface hit M_2 ; therefore, these scanners can only be used in moderate-power systems and after detailed computer simulation of the power densities in the FGR spots. The scanner dimensions can be reduced even further in low-power systems only, because for every set of scanner parameters, both mirrors interact with FGRs from both surfaces. In addition, it is almost impossible to employ extremely large or small meniscus curvatures because of the dramatic decrease in the resulting optical performance.

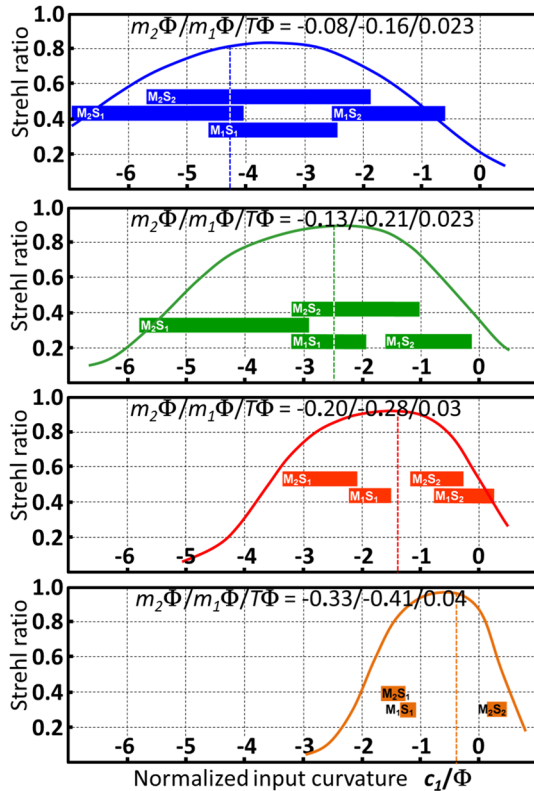


Fig. 8 Computed Strehl ratios (curves) and calculated forbidden input curvatures (horizontal bars) for four simulated scanners with $\Xi_i = 0.33\Phi^{-1}$ and $NA_i = 0.03$. The notations on the bars are described in the text. The dashed vertical lines indicate the estimates given by Eq. (5). The graphs for the first three scanners are represented by separate colors, which also coincide with the colors in Fig. 6. The scanner parameters are given above each curve in the format $m_2\Phi/m_1\Phi/T\Phi$.

Processes that involve cutting of thin polymers, paper, and cardboard, marking of glass and plastics, and skiving (so-called kiss-cutting) of layered composites^{45,46} require lower laser intensities; therefore, significant output NA reduction is possible with the same processing field size. A diagram for choosing the optimization starting point for a scanner with $\Xi_i = 0.33\Phi^{-1}$ and $NA_i = 0.015$ is shown in Fig. 9.

In comparison with Fig. 8, decreasing the NA widens the meniscus curvature range for all investigated scanners, providing high-quality focusing in the processing field. Additionally, the NA is implicit in Eqs. (26) and (27), through the mirror dimensions. Decreasing these dimensions significantly widens the gaps between the forbidden curvature ranges for large scanners with $|m_2|$ from 0.2 to $0.33\Phi^{-1}$ and creates a narrow ghost-free gap for a scanner with $|m_2| = 0.13\Phi^{-1}$. Correspondingly, a decrease in the $x - y$ separation moves the entrance pupil closer to the meniscus, shifting the aplanatism condition [Eq. (5)] to larger curvatures. Basically, the optimal curvature ranges of the menisci of most compact scanners are still overlapped by the forbidden ranges. However, the use of flat or, alternatively, very steep menisci provides quite acceptable focusing quality. Furthermore, the FGR NAs decrease proportionally to NA_i [Eqs. (9) and (15)], yielding a quadratic decrease in the power densities of the FGR spots and significantly

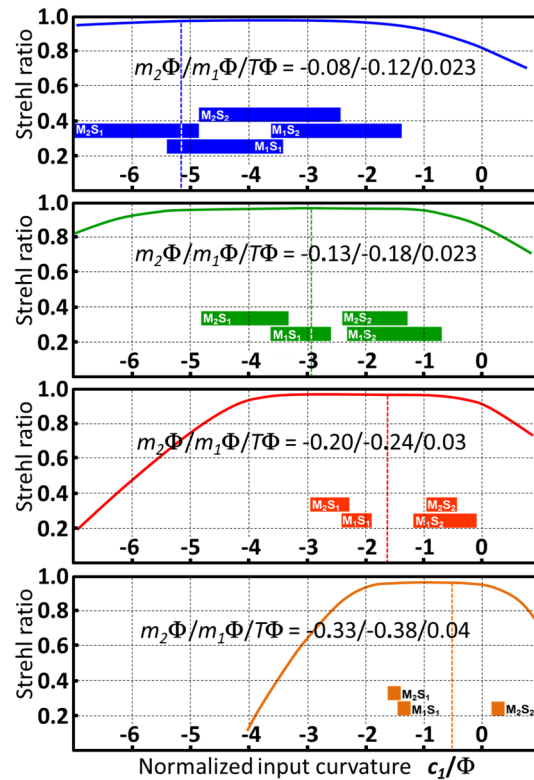


Fig. 9 Computed Strehl ratios (curves) and forbidden input curvatures (horizontal bars) for four simulated scanners with $\Xi_i = 0.33\Phi^{-1}$ and $NA_i = 0.015$. All symbols and notation have the same meanings as in Fig. 8.

relaxing the operating conditions of the mirrors of most compact scanners.

A third application of great practical importance is the processing of bulky materials by beam scanning along a smooth trajectory in a narrow field, for which the object to be processed is mainly moved by another drive. Such beam positioning is used for remote and robotic welding of metals and plastics,^{47,48} for gas-assisted and fusion metal cutting with so-called dynamic beam shaping,⁴⁹ and in infinite-field-of-view systems.^{50,51} Obviously, with dramatic reduction in the processing field size, diffraction quality focusing is provided by lenses with any shape factor, even with significant output NAs. Therefore, for such systems, the scanner is optimized in terms of the FGR field position only. Consider the manner in which the forbidden curvature ranges follow the processing field size changes for the scanner with $m_2\Phi/m_1\Phi/T\Phi = -0.13/-0.21/0.023$ and $NA_i = 0.03$ (green plots from Fig. 8), as an example. Figure 10 demonstrates that, when the processing field size is reduced by a factor of four from $\Xi_i\Phi = 0.33$ to 0.08, sufficiently wide allowed curvature windows appear in the $c_1/\Phi = -1, -2,$ and -3 areas, and the diffraction quality focusing is achieved in the entire investigated curvature range. The bar stack asymmetry is explained by the asymmetry of c_1/Φ and c_2/Φ in the right and left wings. The left wings correspond to meniscus surfaces with larger curvatures. In the right wings, the curvatures are smaller; therefore, FGR fields of considerable sizes exist even for small scanning angles.

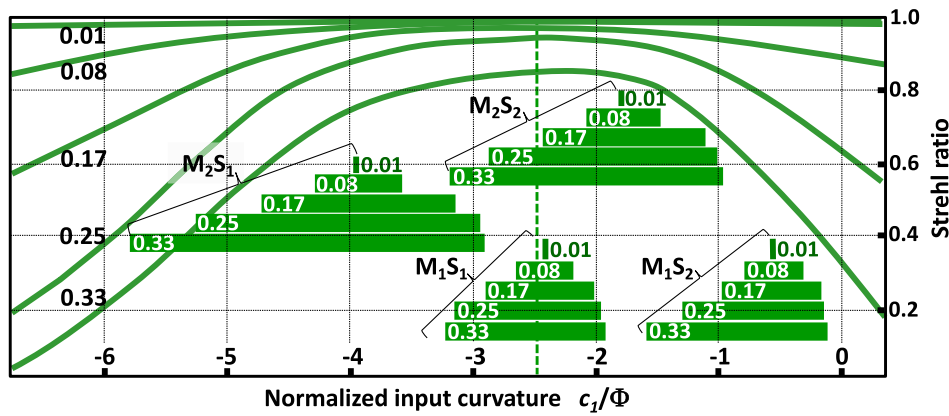


Fig. 10 Computed Strehl ratios (curves) and forbidden input curvatures (horizontal bars) for scanner with $m_2\Phi/m_1\Phi/T\Phi = -0.13/-0.21/0.023$ and $NA_i = 0.03$ versus maximum processing field size. The latter is expressed in units of $\Xi_i\Phi$ and shown in the bars and to the left of the curves. All other symbols and notation have the same meanings as in Fig. 8.

6 Conclusions

An algorithm for determining the starting point for computer optimization of a two-mirror scanner with a meniscus for use in laser technology was developed in this study. Numerical simulations of scanner optical quality were conducted with widely varying parameters. Scanners with fixed and optimized entrance pupil positions were studied. The input parameters of the optimization were the output NA, the optical power (Φ), and a set of scanner mirror characteristics. The major output optimization parameter was the normalized curvature of the meniscus input surface c_1/Φ (where c_1 is the input curvature). A rather narrow curvature range in which the optical quality of a fixed system is identical to that of an optimized one was found to exist. In this range, there are three local values of c_1 for which the nearly aplanatic conditions are spontaneously and alternately fulfilled on the meniscus surfaces. The position of the range center and its width are determined by Eqs. (5) and (6), respectively. Then, optimization of the distance from the meniscus to the scanning mirrors yields a near aplanatic meniscus output surface for all possible c_1/c_2 pairs in a wide range (where c_2 is the output curvature), from extremely steep to flat menisci.

For scanners working with high-power laser sources, optimization with the aim of satisfying the aplanatism conditions is insufficient, because there is high probability of damage to the mirrors by FGRs from the meniscus surfaces, the brightness of which can reach tens of megawatts per square centimeter. A computer simulation of the focusing quality in the FGR fields created for a scanner output NA range of 0.015 to 0.03 and for different scanner geometries showed that, for all configurations, FGR spots from 17- to 100- μm root-mean-square radius exist for at least one of the surfaces, for almost all c_1/c_2 pairs and input angle ranges. Therefore, for medium-power laser sources, possible FGR field location in the scanner mirror space must be addressed via numerical simulation of the FGR spot brightness and comparison of the simulated values with the declared damage threshold of the mirror surface. For high-power sources, the system configuration should completely eliminate the possibility of the FGR fields being located inside the scanner space. Here, the

characteristics of the FGR fields were analyzed to find the starting points for optimization of ghost-free systems. Using the matrix optics approach, analytical expressions were obtained for their dimensions [Eqs. (10) and (16)], positions [Eqs. (8) and (20)], and back-focused ghost NAs [Eqs. (9) and (15)]. By solving a one-dimensional problem of intersection between the mirror and FGR planes, expressions were obtained for the forbidden input curvature ranges, expressed in terms of the scanner input parameters [Eqs. (26) and (27)]. When searching for the starting point for the scanner for a high-power laser, these expressions take precedence over the conditions in Eqs. (5) and (6).

Finally, several variants of scanners used to perform basic laser machining processes at various power levels were considered in detail. The diagrams in Figs. 8 and 9 present the results of computer simulations of the optical beam quality in the processing field, together with the forbidden c_1/Φ ranges for scanners with processing field diagonals approximately equal to their EFLs, different output NAs, and different mirror positions. The diagram in Fig. 10 illustrates that the forbidden curvature ranges become narrower with decreasing processing field size.

In conclusion, this paper demonstrates that compacting a scanner always improves its optical performance, for a fixed output NA. In general, compacting is an alternative to using scanners in systems with high-power laser sources. Therefore, the scanner mirrors in laser systems delivering high-beam brightness over large processing fields should be sufficiently far from the focusing meniscus. The possibility of using compact scanners in such systems arises only when the processing field size is artificially limited to 10% to 20% of the maximum possible value, which is determined by the meniscus EFL. Despite its seeming complexity, the developed algorithm can be used to analyze multi-component systems. For example, splitting a meniscus into two components typically gives a standard configuration in which the ghosts from the second and third surfaces do not have real focuses in the scanner mirror space.

In future research, we will concentrate on studying the practical applications of systems designed using the approaches described herein. Moreover, we will focus on development of compact scanners for high-power lasers,

for which all FGRs can be placed inside the sag of the input quasiconcentric component.

7 Appendix

The equality of the FGR field sizes from both surfaces at a fixed longitudinal coordinate can easily be proven analytically. If we express the NAs in Eq. (7) for the input surface using the input beam size, we obtain $\Xi_j/\Xi_1 = -2c_1/\Phi$. On setting $\Xi_2 = \Xi_1$ in Eq. (16), we find that the input curvature (for which the output curvature is such that $\Xi_2 = \Xi_1$) is equal to $c'_1 = c_1 + n\Phi/(n-1)$. Substituting c'_1 in Eq. (20), we obtain $z_2 = (2c)^{-1} = z_1$. Computer simulations show that, in reality, Ξ_2 exceeds Ξ_1 by no >5% for a thick meniscus. For the considered estimates, such an approximation error is not critical. An approximate equality $-z_j\Phi \approx \Xi_j/\Xi_i$ for FGRs from the first surface of the meniscus is obtained by equating Eqs. (8) and (10), whereas that for FGRs from the second surface is obtained by equating Eqs. (16) and (20), assuming $T = 0$.

Acknowledgments

The authors are grateful for funding from the Government of Russian Federation (Award No. 08-08, Agreement No. 074-11-2018-004). The authors also want to thank Anton Boitsev (ITMO University) for comments on math.

References

- M. J. Kidger, *Intermediate Optical Design*, SPIE Press, Bellingham, Washington (2004).
- W. J. Smith, *Modern Lens Design*, McGraw-Hill, New York (2005).
- L. Shabalina and V. Spiridonova, "Toxicity and character of the effect of some zinc compounds," *J. Hyg. Epidem. Microbiol. Immun.* **32**(4) 397–405 (1988).
- II-VI Infrared, "Zinc Selenide (ZnSe)," <http://www.iivinfrared.com/Optical-Materials/znse.html> (11 July 2018).
- R. Kingslake and R. B. Johnson, *Lens Design Fundamentals*, 2nd ed., SPIE Press, Bellingham, Washington (2010).
- T. Jamieson, "Thick meniscus field correctors," *Appl. Opt.* **21**(15) 2799–2803 (1982).
- N. Zoric et al., "Design of an ultraviolet projection lens by using a global search algorithm and computer optimization," *Adv. Opt. Techn.* **6**(1) 31–38 (2017).
- V. I. Yurevich et al., "Optical design and performance of F-Theta lenses for high-power and high-precision applications," *Proc. SPIE* **9626**, 96261S (2015).
- G. Toesko and C. Dehnert, "Ultrafast laser optics: femtosecond laser optics combat pulse dispersion, color errors, and reflections," *Laser Focus World* **52**(3), 38–40 (2016).
- J. D. Rogers et al., "Removal of ghost images by using tilted element optical systems with polynomial surfaces for aberration compensation," *Opt. Lett.* **31**, 504–506 (2006).
- A. Salama et al., "TEA CO₂ laser machining of CFRP composite," *Appl. Phys. A* **122** 497 (2016).
- S. Heidrich et al., "Glass processing with high power Q-switch CO₂ laser radiation," in *Lasers Manuf. Conf. (LIM 2015)*, Munich, Germany (2015).
- PAR Systems, "Materials processing," <https://www.par.com/technologies/pulsed-co2-lasers/applications/materials-processing/> (11 July 2018).
- S. Ristic et al., "Analysis of ceramics surface modification induced by pulsed laser treatment," *Proc. Appl. Ceram.* **8**(1), 15–23 (2014).
- GAM LASER, Inc., "EX5/EX10 CO₂ TEA Laser," <http://www.gamlaser.com/CO2%20Laser.htm> (11 July 2018).
- R. Sandwell, "TEA CO₂ lasers cut into excimer market," *Industr. Photonics* **3**(3), 12–13 (2016).
- PAR Systems, "Atmospheric TEA CO₂ lasers," <https://www.par.com/technologies/pulsed-co2-lasers/atmospheric-tea-co2-lasers/> (11 July 2018).
- FEHA Lasertec, "MICROSTORM™ laser series," http://www.feha-laser.de/fileadmin/user_upload/2_Aktuelles/FEHA_MICROSTORM__product_flyer_1.pdf (11 July 2018).
- G. Staupendahl, "A novel Q-switched CO₂ laser and its applications," *Lasertechnik J.* **11**(5), 22–25 (2014).
- S. Lee, "Q-switched CO₂ lasers deliver power," *Indus. Laser Solutions* **17**(6) (2002).
- HyperMemo, "Innovative high repetitive rate short-pulsed CO₂ laser," <http://www.hypermemo.eu/technology/short-pulsed-co2-laser/> (11 July 2018).
- V. V. Kiyko and D. A. Mikhaylov, "The control of CO₂ lasing temporal characteristics by modulated self-injected irradiation," *Proc. SPIE* **9729**, 97290N (2016).
- II-VI Infrared, "CO₂ laser consumables," http://www.iivinfrared.com/CO2-Laser-Optics/co2-laser-optics_products.html (11 July 2018).
- Design Research Optics, "CO₂ lenses," <https://www.designresearchoptics.com/co2-lenses> (11 July 2018).
- Ophir Optronics, "Laser lenses," <http://www.ophiropt.com/co2-lasers-optics/laser-lenses> (11 July 2018).
- R. H. Abd El-Maksoud, "Ghost image analysis for optical systems," Thesis for the degree of Doctor of Philosophy, The University of Arizona (2009).
- Cambridge Technology, "Galvanometer XY scanner sets," <http://www.cambridgetechnology.com/products/galvanometer-xy-sets> (11 July 2018).
- Nutfield Technology, "Product selection guide: Galvanometer scanners," <https://nutfieldtech.com/product-guide-galvos> (11 July 2018).
- optoSIC, "Scanning mirrors," <http://www.optosic.de/product-overview.html> (11 July 2018).
- Optics Balzers, "Laser scanning mirrors," <http://www.opticsbalzers.com/en/products/mirrors/laser-scanning-mirrors.html> (11 July 2018).
- Raylase, "2-axis deflection units," <https://www.raylase.de/en/products/2-axis-deflection-unit.html> (11 July 2018).
- Newson NV, "rthor™ smart deflector," <http://www.newson.be/rthor.htm> (11 July 2018).
- Scanlab, "Scan systems," <http://www.scanlab.de/en/products/scan-systems> (11 July 2018).
- W. T. Welford, *Aberrations of Optical Systems*, Adam Hilger, Bristol, Philadelphia & New York (1986).
- M. Born and E. Wolf, *Principles of Optics*, 7th ed., Cambridge University Press, Cambridge (1999).
- H. Gross, "Handbook of optical systems," in *Fundamentals of Technical Optics*, Vol. **1**, WILEY-VCH Verlag GmbH & Co. KGaA, Weinheim (2005).
- H. Gross, "Handbook of optical systems," in *Aberration Theory and Correction of Optical Systems*, WILEY-VCH Verlag GmbH & Co. KGaA, Weinheim (2007).
- S. Maruyama, "On the aplanatic surface," *Proc. Phys.-Math. Soc. Japan*, **22**(4), 320–325 (1940).
- A. Gerrard and J. M. Burch, *Introduction to Matrix Methods in Optics*, John Wiley & Sons, London, New York (1975).
- G. Wairimu, B. W. Ikua, and P. N. Kioni, "CO₂ laser machining of wood, perspex and glass with and without use of assist gas," *Int. J. Sci. Res. Innov. Tech.* **2**(2) 128–133 (2015).
- A. Bresciani, A. Cocquio, and C. Ricci, "Innovative laser cutting process for ceramic slabs," in *XI World Congress on Ceramic Tile Quality*, Castellon, Spain (2010).
- N. K. M. Chaudhari and S. Ketan, "Parametric optimization of CO₂ laser machining on polypropylene—a review," *Int. J. Adv. Research Innov. Ideas Edu.* **2**(3) 2529–2533 (2016).
- M. Nattapat et al., "Laser surface modification of carbon fiber reinforced composites," *Mat. Manuf. Proc.* **30**(12), 1450–1456 (2015).
- J. Serbin and G. Oulundsen, "Lasers improve display glass cutting," *Inf. Display* **33**(5), 38–41 (2017).
- M. Hemmerich et al., "Galvanometer scanning technology and 9.3 μm CO₂ lasers for on-the-fly converting applications," in *Lasers in Manufacturing Conf. (LIM 2017)*, Munich, Germany (2017).
- S. Lee, "CO₂ processing at 9 microns," *Indus. Laser Solutions* **17**(3) (2002).
- Kuka, "CO₂ laser robots," <https://www.kuka.com/en-de/products/production-systems/standard-products-for-automation/co2-laser-robots> (11 July 2018).
- TRUMPF, "Scanner welding: highly productive processing with no downtime," https://www.trumpf.com/en_US/applications/laser-welding/scanner-welding/ (11 July 2018).
- C. Goppold, T. Pinder, and P. Herwig, "Dynamic beam shaping for thick sheet metal cutting," in *Lasers in Manufacturing Conf., (LIM 2017)*, Munich, Germany (2017).
- Aerotech, "Infinite field of view (IFOV) synchronizes linear or rotary servo axes with laser scanners," <https://www.aerotech.com/product-catalog/software/automation-3200-software/infinite-field-of-view-ifo-v.aspx> (11 July 2018).
- Polaris Motion, "Motion control system catalog," http://pmdi.com/upload/docs/PolarisCatalogOct2017_Web.pdf (11 July 2018).

Vladimir I. Yurevich received his PhD from the Institute for Fine Mechanics and Optics at St. Petersburg in 1989. He worked for the IFMO and for St. Petersburg University. He joined the Laser

Center in 2000 as a head of the laser and optics department. He also holds a position at ITMO University. His research interests include lasers and beams, optical design, and laser-matter interaction. He has published 40 papers and holds 8 patents.

Sergey Gorny is the director of the Laser Center Ltd. He received his PhD from the Polytechnic Institute at St. Petersburg in 1986. He is the

author of more than 130 papers. His current research interests include laser machining and laser-matter interaction. He also actively works for Peter the Great St. Petersburg Polytechnic University.

Biographies of the other authors are not available.